


# Tin removal by an annular surface wave plasma antenna in an extreme ultraviolet lithography source


Cite as: J. Appl. Phys. **132**, 113302 (2022); <https://doi.org/10.1063/5.0094375>

Submitted: 02 April 2022 • Accepted: 12 August 2022 • Published Online: 16 September 2022

 Dren Qerimi,  Andrew C. Herschberg, Gianluca Panici, et al.

## COLLECTIONS

 This paper was selected as Featured

 This paper was selected as Scilight



View Online



Export Citation



CrossMark

## ARTICLES YOU MAY BE INTERESTED IN

[In-situ cleaning technique improves extreme ultraviolet lithography efficiency](#)

Scilight **2022**, 381113 (2022); <https://doi.org/10.1063/10.0014100>

[Study of a linear surface wave plasma source for tin removal in an extreme ultraviolet source](#)

Journal of Vacuum Science & Technology B **38**, 052601 (2020); <https://doi.org/10.1116/6.0000200>

[Effects of thin metal contacts on few-layer van der Waals ferrielectric  \$\text{CuInP}\_2\text{S}\_6\$](#)

Journal of Applied Physics **132**, 114102 (2022); <https://doi.org/10.1063/5.0096704>



## Time to get excited.

Lock-in Amplifiers – from DC to 8.5 GHz



[Find out more](#)



# Tin removal by an annular surface wave plasma antenna in an extreme ultraviolet lithography source



Cite as: J. Appl. Phys. **132**, 113302 (2022); doi: [10.1063/5.0094375](https://doi.org/10.1063/5.0094375)

Submitted: 2 April 2022 · Accepted: 12 August 2022 ·

Published Online: 16 September 2022



Dren Qerimi, Andrew C. Herschberg, Gianluca Panici, Parker Hays, Tyler Pohlman, and David N. Ruzic<sup>a)</sup>

## AFFILIATIONS

Department of Nuclear, Plasma, and Radiological Engineering, Center for Plasma-Material Interactions, University of Illinois at Urbana-Champaign, 216 Talbot Lab, 104 S. Wright St., Urbana, Illinois 61801, USA

<sup>a)</sup>Author to whom correspondence should be addressed: [druzic@illinois.edu](mailto:druzic@illinois.edu)

## ABSTRACT

Tin contamination of the collector mirror surface remains one of the crucial issues of EUV (Extreme Ultraviolet) sources, directly impacting the availability of the tool. Hydrogen plasma-based tin removal processes employ hydrogen radicals and ions to interact with tin deposits to form gaseous tin hydride ( $\text{SnH}_4$ ), which can be removed through pumping. An annular surface wave plasma (SWP) source developed at the University of Illinois—Urbana Champaign is integrated into the cone and perimeter of the collection mirror for *in situ* tin removal. The SWP is characterized by high ion and radical densities, low electron temperature, and local generation where etching is needed. This method has the potential to significantly reduce downtime and increase mirror lifetime. Radical probe measurements show hydrogen radical densities in the order of  $10^{19} \text{ m}^{-3}$ , while Langmuir probe measurements show electron temperatures of up to 6 eV and plasma densities on the order of  $10^{17-18} \text{ m}^{-3}$ . The generated ions are essential to the tin cleaning and have sufficiently low energy to cause no damage to the collector capping layer. Tin etch rates of up to 270 nm/min were observed in a variety of experimental conditions, including various powers, pressures, flowrates, and temperatures. The high etch rates demonstrated in this study exceed the expected contamination rate of the EUV source.

Published under an exclusive license by AIP Publishing. <https://doi.org/10.1063/5.0094375>

## I. INTRODUCTION

Extreme ultraviolet lithography (EUVL) has recently been incorporated in high-volume manufacturing after decades of research and development. Extreme ultraviolet light is generated when molten tin (Sn) droplets are hit by a  $\text{CO}_2$  laser to produce the hot laser-produced-plasma (LPP), ionizing tin up to the 12+ state.<sup>1,2</sup> The 13.5 nm EUV photons, which are released during the Sn de-excitation process, are collected and directed toward the lithography exposure tool via collector optics.<sup>3</sup> In order to be reliable, the EUV sources must meet specifications of five parameters: power, spectral content, etendue, dose stability, and collector lifetime.<sup>4,5</sup> While EUVL has reached high-volume manufacturing, tools still have engineering issues to resolve.

Among such issues is tin deposition which contaminates the EUV source and decreases the reflectivity of the collector mirror.<sup>6</sup> Contamination occurs in the following process: once the plasma is created by the laser, atomic tin vapor is created and has to go

somewhere. This tin vapor collects on surfaces and builds up. Sometimes, the molten tin gets thick enough in some places to fall and deposit in even more major quantities, but generally unmitigated deposition would be on the order of a few nm per minute. Additionally, high-energy ions and neutrals from the plasma can bombard the collector and damage the multilayer mirror (MLM).<sup>7</sup> EUV mirrors have a reflectivity of less than 70%; thus, strict requirements are followed in order to maintain uptime of the machine because collector lifetime is related to cost-of-ownership and economic viability. Even 1 nm of tin on a collector can degrade the reflectivity by 10%. The current target for EUV sources is 30 000 h of uninterrupted operation.<sup>8,9</sup> The conversion efficiency of EUV light is directly related to collector lifetime because reflectivity loss impacts the rest of lithographic process, hindering the tool's ability to manufacture chips.<sup>5</sup>

To mitigate tin debris inside the source, very high flow rates of hydrogen gas are needed. Hydrogen gas pressure, usually around

200 Pa, determines tin-ion stopping power<sup>3,10</sup> and attempts to direct the tin vapor away from the mirror. Hydrogen gas has a secondary role, acting as a buffer gas to reduce ion energy and flux from reaching the mirror surface.<sup>11,12</sup> Nevertheless, tin accumulates over time, contaminating the EUV source.<sup>13</sup> Current methods of tin mitigation in an EUV source consist of replacing the collector and cleaning it remotely with the help of hydrogen radicals.<sup>14</sup> While this method works, it significantly contributes to the downtime of the EUV machine. The continued increase in demand for manufactured chips requires that lithography tools have the capability to operate with minimal disruption.

A new cleaning technique developed at University of Illinois has shown promising results due to its ability to generate hydrogen radicals *in situ*, eliminating the need to replace the collector in EUV source.<sup>15</sup> This technique utilizes a surface wave plasma (SWP), which generates high densities of hydrogen radicals and ions, yielding an etch rate up to 270 nm/min, far exceeding tin deposition rates on the source surfaces.<sup>16</sup> The advantage of the surface wave plasma is the ability to generate hydrogen radicals and atoms at the desired etching locations, thus enabling *in situ* etching in the EUV source during operation. Semi-circular SWP sources were used to determine tin etch rates and radical densities in order to maximize etch rates. A series of tests were conducted with semi-circular antennas in a coupon collector to understand plasma expansion along the collector surface with respect to power, hydrogen flow rate, and collector surface temperature. In addition, a secondary arc antenna is integrated in the perimeter of the collector and tested with varying pressure. At lower pressure regimes, plasma coverage increases; given adequate input power, the goal is to eventually cover the entire collector surface with SWP.

## II. EXPERIMENTAL

The Tin Removal Experiment (TRES) chamber is an ASML NXE:3100 EUV source chamber in which etch experiments were conducted under real EUV source conditions. The TRES chamber is equipped with four dry pumps capable of pumping 44 SLM each and a 1600 l/s turbo-molecular pump. A linear motion feedthrough is attached via a 4.5-in. flange which holds a Langmuir probe and radical probes used for plasma diagnostics along radial directions. The system can flow 150 SLM of hydrogen and has a base pressure in the low  $10^{-4}$  Torr range. Flow is directed from the center of the collector also known as the cone and from the perimeter of the collector. Figure 1 shows the chamber schematics and chamber. Outside the TRES chamber, the SWP antennas are connected to microwave power supplies capable of delivering 100 W each. Microwave power delivery is optimized by using a stub tuner as a manual matching network. A back flange holds the NXE:3100 coupon collector which is equipped with three cooling channels which spiral in opposite directions from and into the center of the collector. Cooling channels help control the temperature of the collector surface. An annular ring antenna is integrated in the cone area of the coupon collector and another arc antenna is integrated in the perimeter of the collector. Both antennas have an inner conductor covered by an alumina. The annular antenna in the cone consists of two semi-circular antennas to generate plasma all around the cone and the arc antenna in the perimeter of the

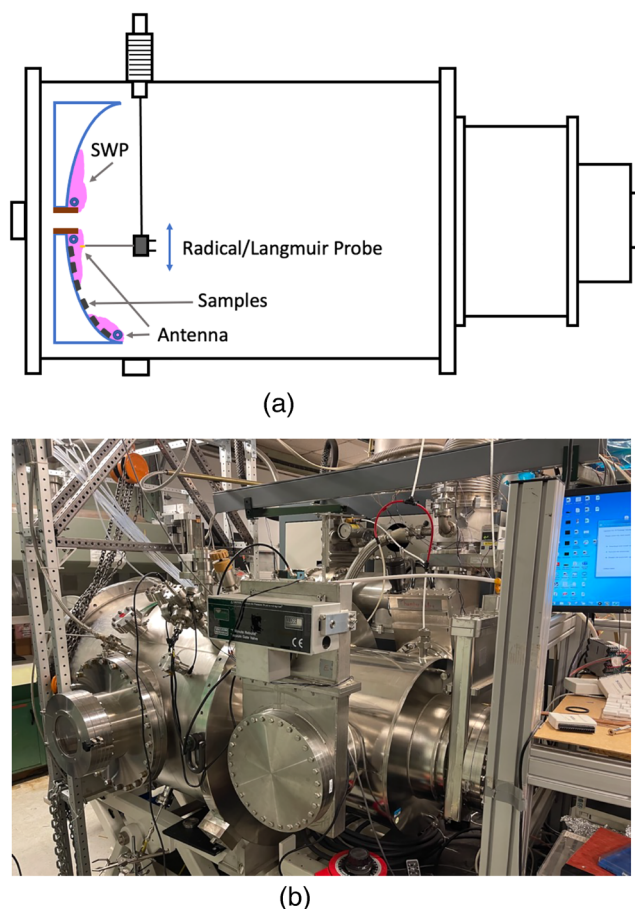
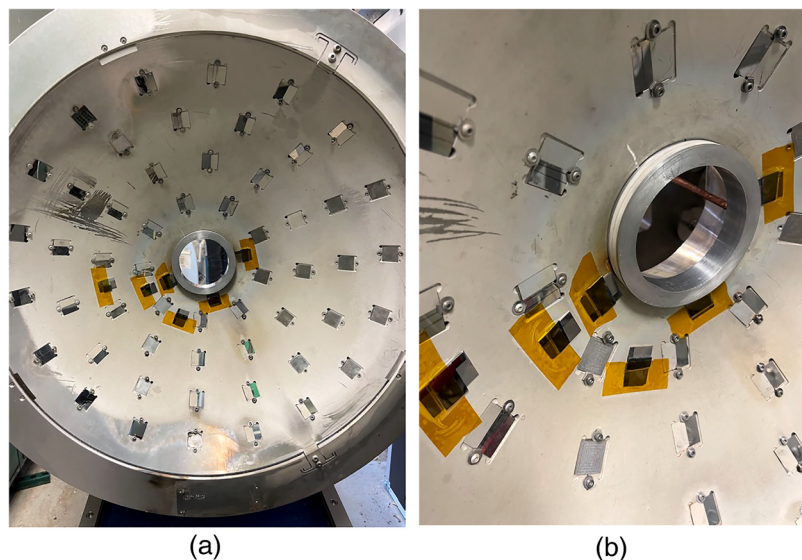


FIG. 1. (a) TRES chamber schematics with coupon collector. (b) A picture of the TRES chamber setup.

collector, as the name suggests, consists of only an arc. The construction of SWP antenna is as follows: two macor (machinable ceramic) rings are machined in a circular shape with a groove in the middle to accommodate the inner conducting copper rings. Two macor rings are closed and their inner surfaces flush against each other to create a seal. An upper outer aluminum ground casing is threaded to a bottom outer aluminum ring in order to enforce the seal of two macor rings as well as to force plasma to radiate only radially. The aluminum ground casing is mounted in the cone of the collector, and it is precisely machined to a snug fit, see Figs. 2 and 3(a). RG 401, a semi-rigid coaxial cable, is responsible to deliver power to the antenna. The microwave power supply is located outside the chamber, and it is connected to a stub tuner which acts as a matching network. The stub tuner is connected to an N-type cable, and the N-type cable is connected to the RG401 launcher via a custom-made N-type connector. RG401 enters the TRES chamber via  $\frac{1}{4}$ -in. ultra-torr feedthrough mounted in a 3 in.-thick Plexiglas slab which is bolted to the main collector flange, see Fig. 3(b). Finally, the RG401 is stripped on the other



**FIG. 2.** Annular SWP antenna installed in the coupon collector with a few half-masked tin-coated silicon samples installed.

end and feed in between the two macor rings to minimize connecting points and, thus, increase delivery efficiency. The RG 401 is connected via threading to the bottom outer aluminum case to minimize any potential gas in which plasma can strike, refer to Fig. 3 for more visual details. Note that this construction ensures a  $50\ \Omega$  load throughout, and the match is set such that the reflected power is for all intents and purposes, zero, or at least below 0.1 W. Tin-coated silicon samples are placed radially from the cone ( $r = 0\text{ cm}$ ) to the perimeter ( $r = 23\text{ cm}$ ). Figure 2 shows the annular SWP antenna in the cone and the half-masked samples installed before an etch test. Etch tests were conducted with varying pressure, power, flow rate, and surface temperature. Each test lasts about 15 min with some exceptions.

A compensated Langmuir<sup>17</sup> and radical probes<sup>18,19</sup> scan radially to measure electron density, ion density, electron temperature, and hydrogen radical density at each sample location, see Fig. 4 for the circuit schematics of compensated Langmuir probe. Silicon samples are coated in a magnetron sputtering chamber at CPMI (Center for Plasma and Material Interactions). Tin deposition on silicon samples occurs before etch test takes place to avoid the creation of oxide layers on tin film. Etch step is measured using a 3D optical profilometer, and post-processing of the data occurs immediately after the etch is tested to minimize the formation of the oxide layers.

### III. RESULTS AND DISCUSSION

Several tests were carried out in the Illinois NXE:3100 EUV source vessel in order to determine the etch rates and to diagnose plasma parameters such as hydrogen electron, ion, and radical density by varying pressure, power, flow rate, and temperature. This experimental setup replicates very closely real EUV source conditions but without the laser system. In Figs. 5(a) and 5(b), two semi-circular antennas were integrated in the cone by

using ceramic to case the conducting antenna wires. Note that the plasma coverage extends all the way around the cone. In Figs. 5(c) and 5(d), an arc antenna was installed in the perimeter of the collector in addition to one semi-circular cone antennas facing the arc antenna. In an actual application to an EUV source, eight antennas would be needed for complete coverage—two in the central cone and six around the perimeter. That number is determined by the etching results as a function of distance from the source as described later in this section. The difference between (5a) and (5b) [and (5c) and (5d)] is the operating pressure—1.3 and 1.5 Torr, respectively. The values were chosen to mimic those used in a real source. Only a very slight difference is discernable in the two cases. Slightly less plasma coverage is seen at the higher pressure cases. Figure 6 schematically shows the location of the samples to be etched and the placement of the antennas for the subsequent experimental results.

Plasma characterization tests were conducted without the tin-coated samples being present. Six sample locations along the radius of the collector were measured with Langmuir and radical probes. The first set of tests was run with varying pressure, going from 0.25 to 1.5 Torr with 0.25 Torr increments while keeping the flow rate and power constant. The second set of tests was run with varying power, going from 25 to 100 W with 25 W increments while keeping the pressure and flow rate constant. The third set of tests was run by varying flow rate, going from 5 to 70 SLM while keeping the pressure and power constant. These values are the total flow rate in the chamber which is the sum of flow rate going through the cone of the collector and the perimeter of the collector. The 5 SLM case is considered to be a zero flow case since the pumps cannot be throttled completely and some flow must be maintained to keep the pressure constant. The total flow rate of a EUV system is on the order of 500 SLM. The fourth set of tests was run by varying collector surface temperature while keeping flow rate, power, and pressure constant. Temperature-dependent tests



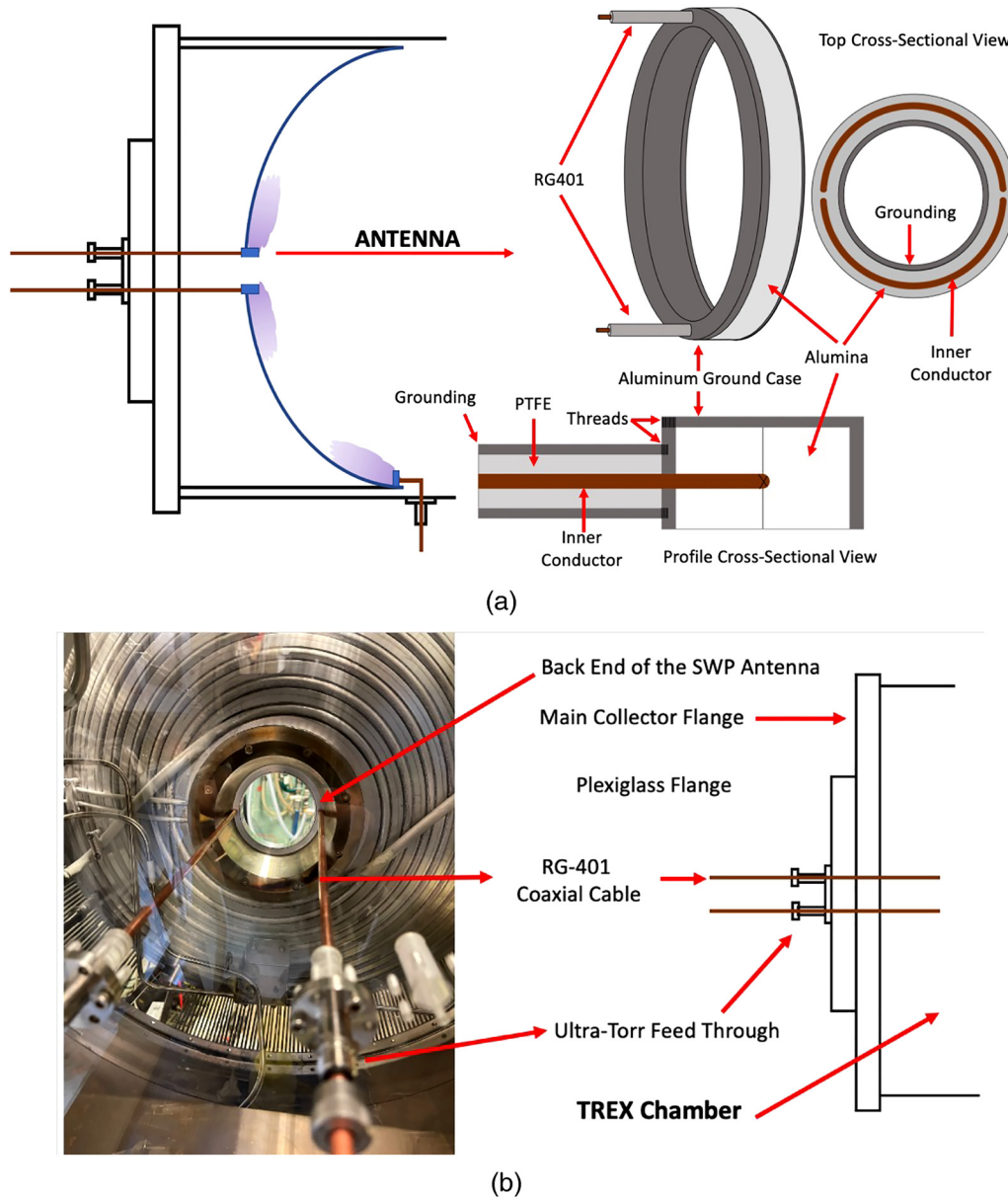


FIG. 3. Schematics of semi-circular SWP antenna which is used in the center cone structure.

were considered only for tin etching experiments and not for plasma diagnostics since the substrate temperature does not affect ion densities and electron temperature. It is worth noting that Langmuir probe measurements were obtained only in the areas closest to the antenna where the SWP is located. Further away in the radial direction there is no visible plasma, and the probe could not collect sufficient current for an accurate measurement.

Langmuir probe measurements of ion density and electron temperature with varying power are shown in Fig. 7. In these

measurements, the Langmuir probe is located in the visible plasma region close to the antenna. As power increases from 25 to 100 W, the electron temperature increases from 1.3 to 2.6 eV. Also, an increase in electron density is observed with power increase since more power delivered creates more plasma and it expands it over a large surface area. Figure 8 shows the plasma parameters with varying hydrogen flow rate, and as has been observed before, there is not much change when flow rate goes from 5 to 70 SLM. Electron temperature is 2.5 eV. Plasma density has a nonsignificant

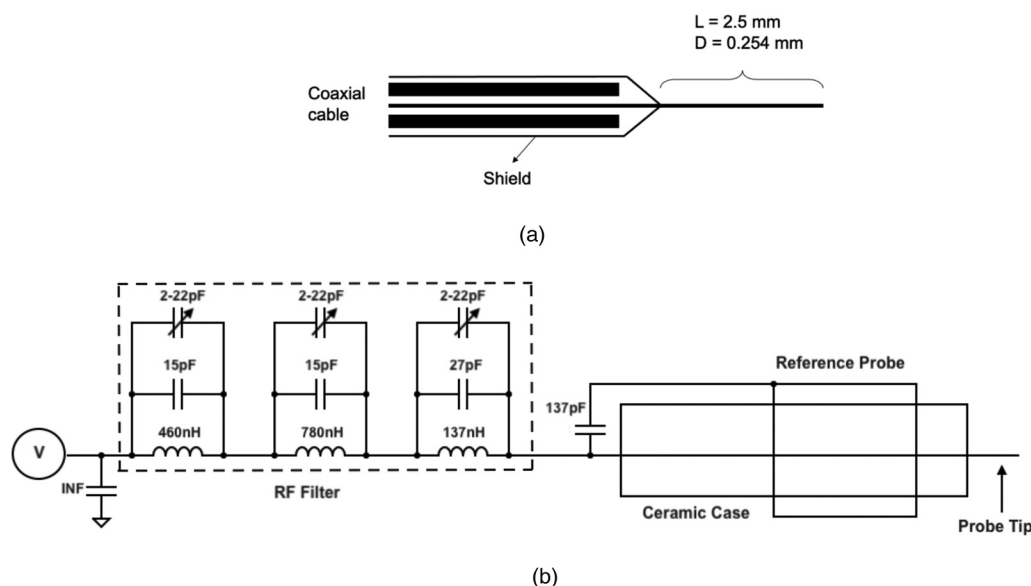


FIG. 4. Circuit schematics of compensated Langmuir Probe.

increase with increasing flowrates. Finally, Fig. 9 shows Langmuir probe measurements with varying pressure. Electron temperature decreases with pressure increase since the mean free path decreases and electrons undergo a higher number of collisions and lose energy in the process. Higher energy electrons will generate more ionization and a larger plasma radius so the plasma density decreases with pressure as well.

Radical probe measurements were carried out for all six sample locations since radicals created by the intense plasma diffuse beyond visible plasma. Figure 10(a) shows radical density with varying power while flow rate is set at 20 SLM and pressure is constant at 1.5 Torr. When power increases from 25 to 100 W, hydrogen radical density increases by an order or magnitude at the closest antenna location. As the distance from the antenna increases, so does the radical density for all four power cases. It is observed that for the 100 W case, the plasma coverage is larger, and density decreases slowly compared to other cases and it is an interesting phenomenon that radical probes detect radicals far away from visible plasma at 23 cm. Figure 10(b) shows the behavior of radical density with varying hydrogen flow rate. As the case of Langmuir probe measurements, there does not seem to be any relationship between flow rate and radical density besides the fact that being further away from plasma, density drops exponentially. Figure 10(c) shows the hydrogen radical density with varying pressure going from 0.25 to 1.5 Torr. At lower pressure regimes, plasma coverage is increased, and, thus, the radical density is higher at locations further down in the collector showing a direct relationship with etch rates.

After plasma characterization was complete, etch tests were carried out under the same experimental conditions. A series of tests were conducted with two semi-circular antenna configurations. The first case was where two semi-circular antennas were

embedded in the cone. Figure 11(a) shows the relationship of etch rate with power. The etch step was measured via 3D optical profilometry in all the samples. In the analysis process, we measured the average height of three different areas in the etched part of the sample and the average height of three different areas in the non-etch part of the sample. The average difference between the etched and non-etched is regarded as the step height. At higher powers, etch rate is higher and it has a behavior similar to hydrogen radical density case with respect to power. Highest etch rate of 208 nm/min is observed at 100 W with sample location closest to the antenna. It is significant to note that 25 W increments yield substantial increase in etch rate with the lowest power of 25 W generating 42 nm/min etch rate at  $r = 0$  cm. The etch rate decreases exponentially with radius increase and this behavior is observed for all experimental settings. Figure 11(b) shows etch rates with varying flow rate, and as was the case for Langmuir probe and radical probes, no changes are noticed. The highest etch rate of 226 nm/min being for the 50 SLM case. Figure 11(c) shows the relationship of etch rate with pressure. The highest etch rate for all test cases is 274 nm/min at 0.25 T for  $r = 0$  cm. As the pressure and radius increases, the etch rate decreases for each pressure range.

Figure 11(d) shows etch rate with respect to collector surface temperature. Note that material migration through Sn being turned into  $\text{SnH}_4$  and then redepositing is not expected to be a major problem on clean surfaces as long as temperatures are below 40 °C.<sup>20</sup> As previously explained in the surface temperature kinetic etch model,<sup>21</sup> the hotter the collector surface the smaller the etch rate is. While keeping pressure, power, and flow rate constant, the difference between the lowest and hottest temperatures is 40 nm/min. The etch rate difference is maintained for the first four samples and the last two do not show any change as it is the behavior for all cases when the etch rates take place further away from

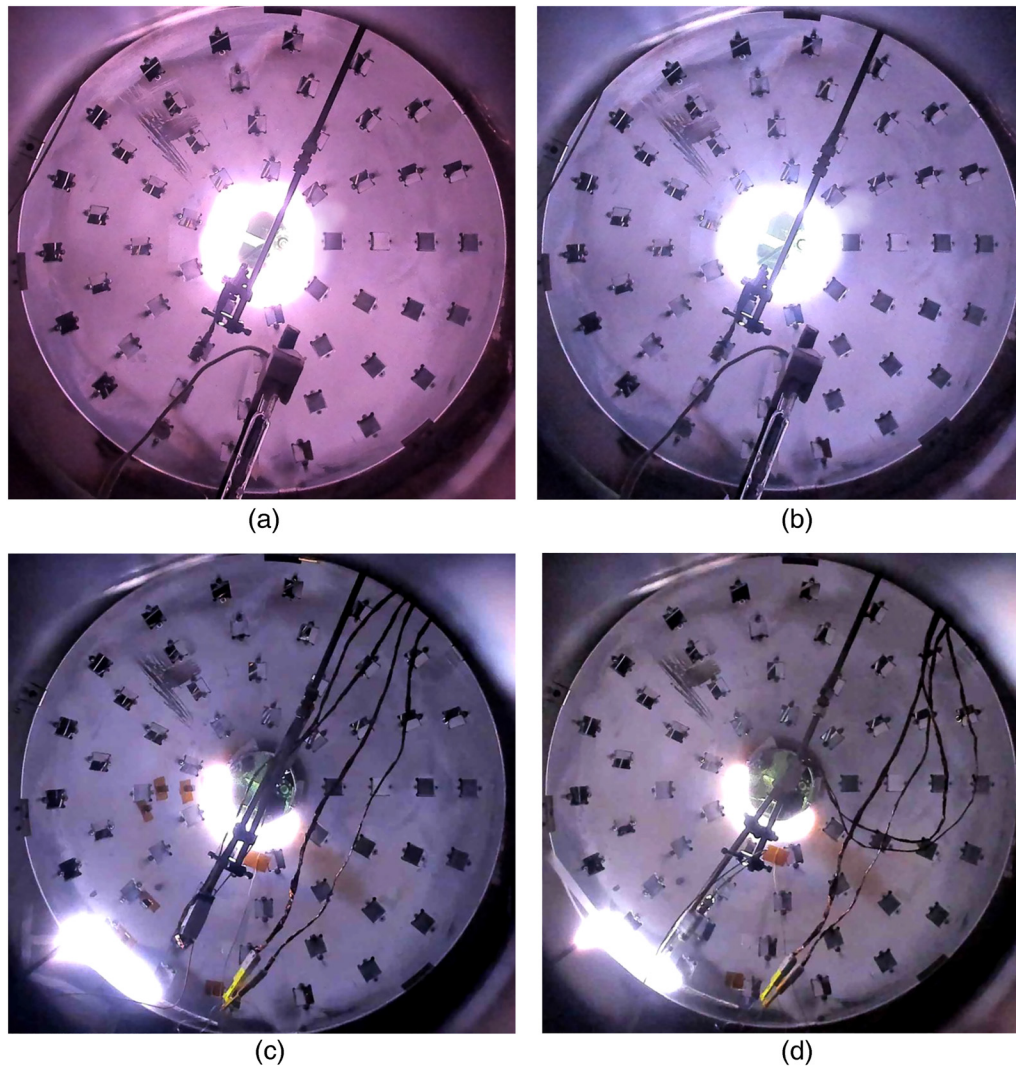


**FIG. 5.** Operating annular SWP source in the NXE3100 chamber at Illinois on a “Coupon” collector at power 100 W per launcher and a hydrogen flow rate of 20 SLM. (a) Dual SWP antenna embedded in the cone operating at 1.3 Torr. (b) Dual SWP antenna embedded in the cone operating at 1.5 Torr. (c) Single semi-circular cone antenna and a single perimeter arc antenna operating at 1.3 Torr. (d) Single semi-circular cone antenna and a single perimeter arc antenna operating at 1.5 Torr. Note that the plasma extends all the way around the cone in cases (a) and (b). Also note that the higher pressure cases show just slightly less plasma coverage.

the antenna. Figure 12 shows the tin etch rate measurements using one semi-circular SWP antenna and a perimeter arc antenna with varying pressure. While the visible SWP did not cover the entire surface area between the cone and perimeter of the collector, there was significant etching all the way across. Cone and perimeter antennas were set at 100 W and the etch rate displays a convex shape behavior, going from a high etch rate near the cone, decreasing in the middle, and then going up near the collector perimeter. From previous experience, it is known that higher power yields higher etch rates and no changes are observed with varying flow rate.<sup>21</sup> Therefore, only cases with varying pressure are considered. Similar to results of Panici *et al.*,<sup>22</sup> at lower pressure regimes, the

etch rate is higher since plasma surface coverage increases; however, it not sufficient to cover the entire collector with visible plasma. Etch rates of around 200 nm/min are observed for both ends of the collector when pressure is 1.5 Torr and the etch rate in the middle sample is increased such that even at 1.5 Torr, the etch rate is around 40 nm/min. Thus, a sufficient etch rate can be achieved over the entire collector.

#### IV. MODELING OF SURFACE WAVE PLASMA

A COMSOL model was built to validate the experimental findings of the surface wave plasma with respect to electron density,

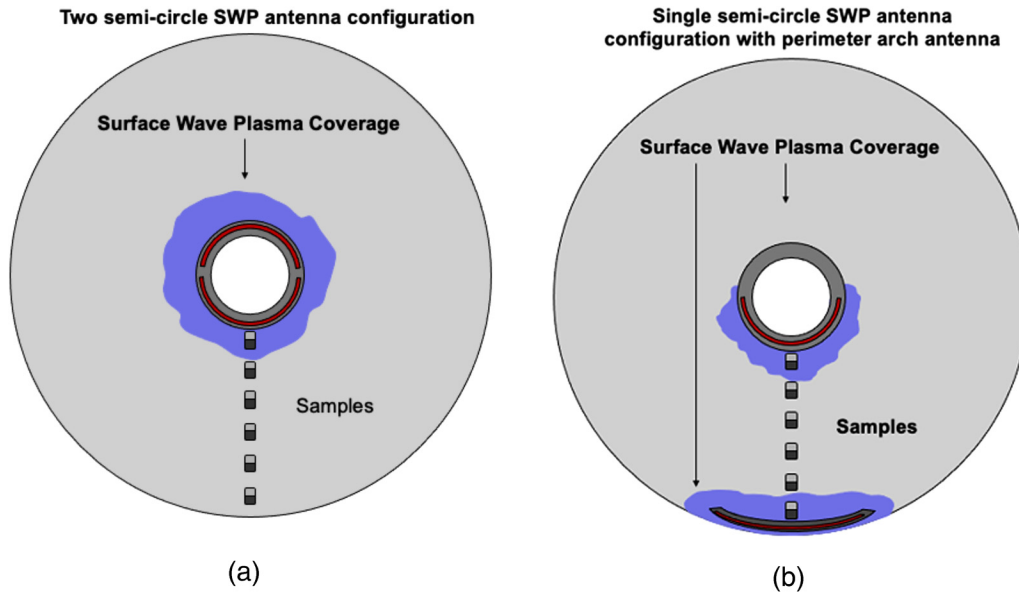


**FIG. 6.** Antenna configurations for SWP sources: (a) two semi-circular cone antennas and (b) one semi-circular cone antennas with one perimeter arc antenna. These are the schematics for the plasma shown in Fig. 5.

electron temperature, and hydrogen radical density. Utilizing the geometry builder in COMSOL, a cross-sectional view is built, see Fig. 13(a), where the grounded collector is located on the bottom part of the picture shown with the same gray color as the upside L-shaped grounded aluminum casing. Aluminum is chosen as the material for the collector extending for half the distance of the collector. The antenna ring is the small brown circle encompassed by the macor rings shown in white and the blue colored area is the domain for which the model is solved. The inner conductor is the 1/8-in. copper ring similar to the actual antenna. The domain is

meshed using triangular elements with more emphasis along the boundary conditions, see Fig. 13(b). Minimum element size for the mesh is  $5 \times 10^{-7}$  m and the maximum element is 0.05 m. PARADISO direct solver is used to run the simulation. COMSOL was used since it allows user defined functions and has been used extensively in our previous work.

In terms of physics, the electron density is calculated by solving coupled drift-diffusion equations where mass and energy transport are separated into electrons and non-electron particles. Due to their smaller mass, electrons respond faster to the incoming

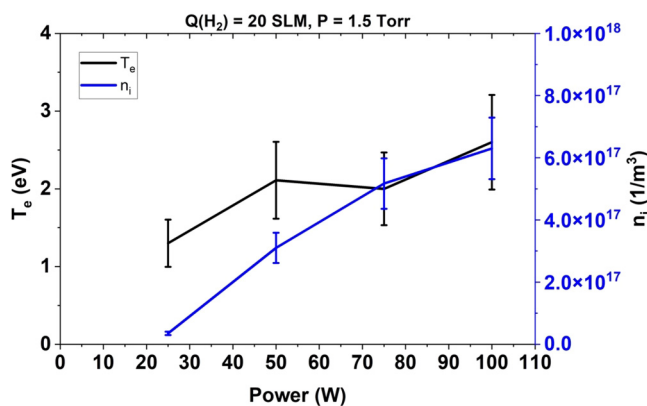


**FIG. 7.** Langmuir probe measurements of electron temperature and ion density with varying power at 1.5 Torr of hydrogen and a 20 SLM flow rate.

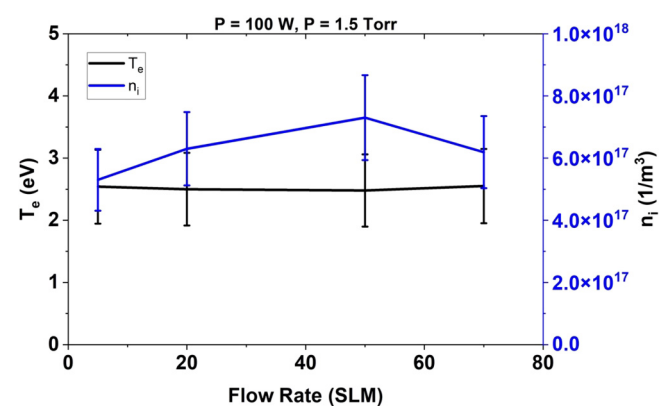


**FIG. 8.** Langmuir probe measurements of electron temperature and ion density with varying hydrogen flow rate at 100 W and 1.5 Torr of hydrogen.



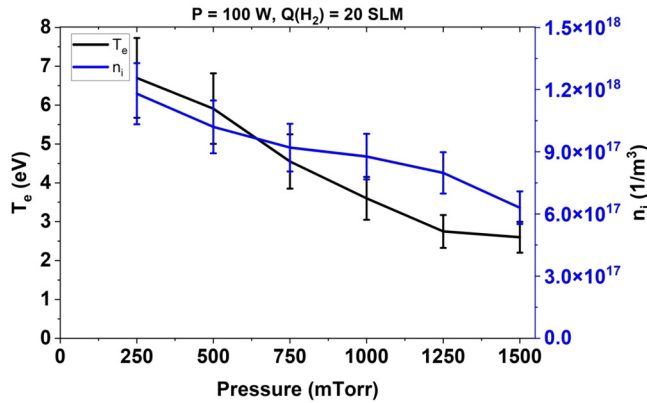


FIG. 9. Langmuir probe measurements of electron temperature and ion density with varying pressure at a power of 100 W and flow rate of 20 SLM.

RF waves whereas ions respond only to bulk electric field which is determined by the plasma space charge,<sup>23</sup>

$$\frac{\partial}{\partial t} n_e + \nabla \cdot [-n_e(\mu_e \cdot E) - D_e \cdot \nabla n_e] = R_e, \quad (1)$$

$$\frac{\partial}{\partial t} n_e + \nabla \cdot [-n_e(\mu_e \cdot E) - D_e \cdot \nabla n_e] + E \cdot \Gamma_e = R_e, \quad (2)$$

$$D_e = \mu_e T_e, \quad \mu_e = \frac{5}{3} \mu_e, \quad D_e = \mu_e T_e, \quad (3)$$

$$\rho \frac{\partial w_i}{\partial t} + \rho(u \cdot \nabla) w_i = \nabla \cdot j_i + R_i, \quad (4)$$

$$\sigma = \frac{n_e q^2}{m_e (v_m + j\omega)}, \quad (5)$$

where  $R_e$  is the electron source,  $R_e$  is the energy loss due to inelastic collision, “ $e$ ” represents the electron transport equation, and “ $\epsilon$ ” represents the electron energy.  $\mu$  is the electron mobility/energy mobility,  $\Gamma$  is the electron flux, and  $D$  is the electron diffusivity/energy diffusivity. Equation (3) shows that electron mobility can be used to calculate electron diffusivity, energy mobility, and energy diffusivity. In this model, plasma is assumed to be collisional and gas is weakly ionized for a given pressure of 1 Torr of hydrogen. Ionization fraction is less than 1% since maximum plasma density is around  $10^{18}/m^{-3}$  and total gas density is on the order of  $10^{22}/m^{-3}$ . In terms of non-electron species, Eq. (4) is used to solve for mass fraction of each individual species  $i$ , where  $u$  is the fluid vector,  $j_i$  is the diffusive flux vector,  $R_i$  is the rate term, and  $w_i$  is the mass fraction. The plasma physics is closely related to the EM since surface wave plasmas are basically described by EM theory.<sup>24,25</sup> Maxwell equations<sup>26–28</sup> are used to describe the plasma module and plasma conductivity is given by Eq. (5), where  $\sigma$  is the

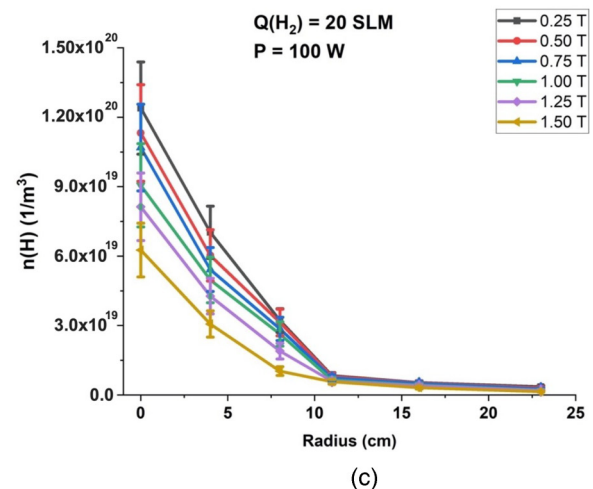
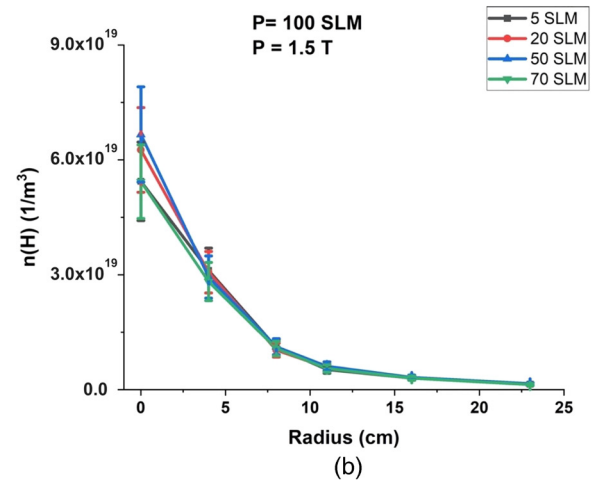
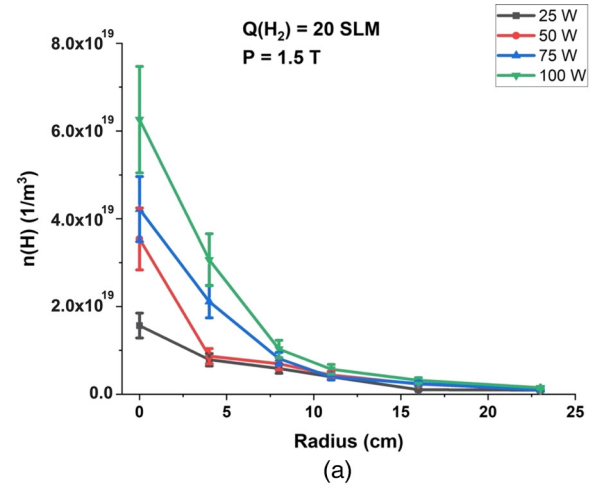
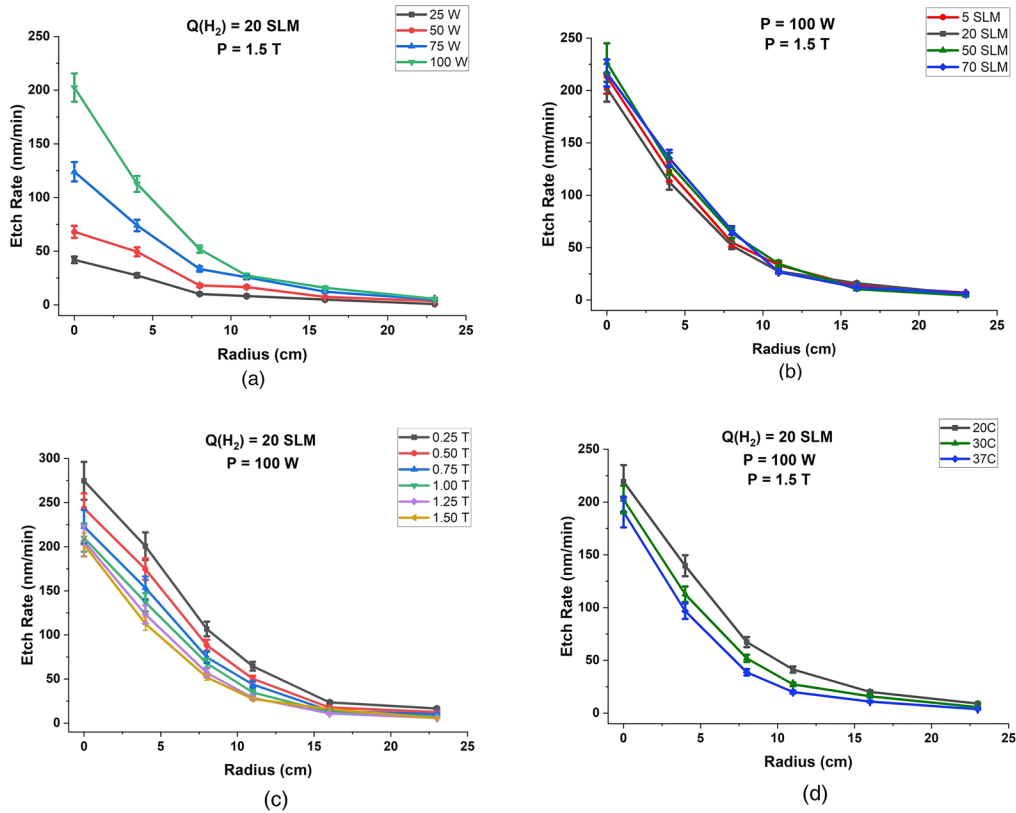


FIG. 10. Hydrogen radical density with varying (a) power, (b) flow rate, and (c) pressure.



**FIG. 11.** Tin etch rate measurements of two semi-circular SWP sources embedded in the cone with varying (a) power, (b) flow rate, (c) pressure, and (d) surface temperature.

plasma conductivity,  $m_e$  is the electron mass,  $q$  is the electron charge, and  $v_m$  is the momentum transfer of background hydrogen and electrons. The aluminum ground casing, collector, and the ring are set as perfect conductors. An input power of 100 W and the 650 MHz frequency are fed in the ring and the RF wave propagates in a TEM mode in a circular direction since the domain is a cross-sectional view of the cylindrically symmetric 3D system. The electrostatic field is solved via Eq. (6) and space charge density  $\rho$  is computed from the plasma chemistry in the model which in this case is taken from Table I. In addition, surface reactions are shown in Table II,

$$-\nabla \cdot \epsilon_0 \epsilon_r \nabla V = \rho. \quad (6)$$

The Local Field Approximation (LFA) helps to solve for ion temperature, which otherwise would have been determined from the gas temperature. Piskin *et al.*<sup>37</sup> shows LFA assumes local velocity distribution of species is balanced with local electric field such that quantities such as ion temperature or mobility can be written with respect to a reduced electric field  $E_r$  as shown in Eq. (7), and ion temperature can be solved by implementing LFA, see Eq. (8),

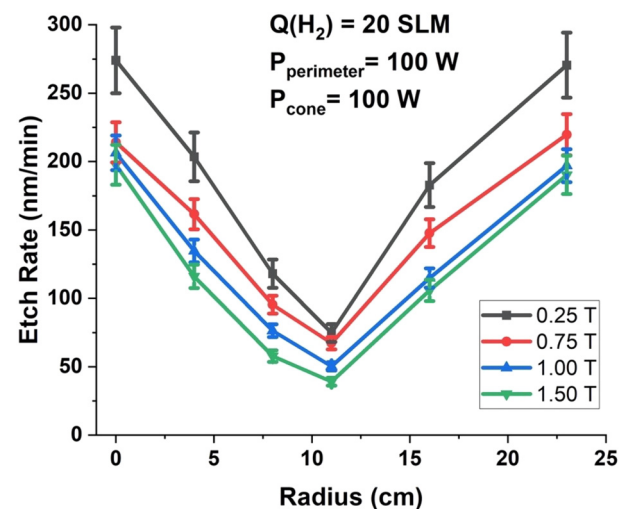


**FIG. 12.** Tin etch rate measurements of one semi-circular SWP sources in the cone and a perimeter arc antenna with varying pressure. Note that the entire surface of the collector can be etched at a rate of at least 40 nm/min.

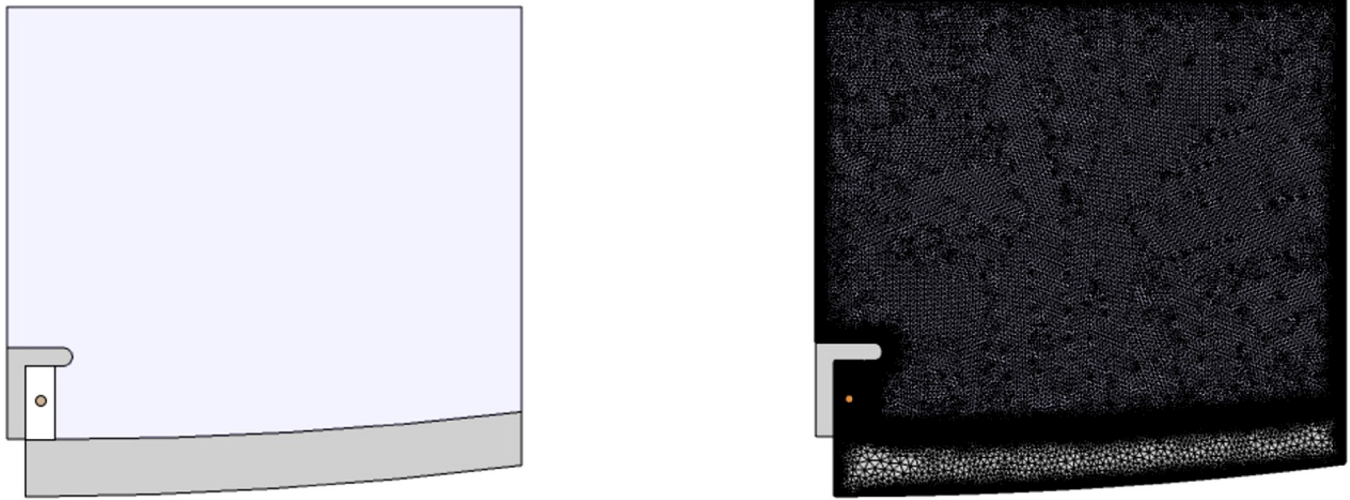


**FIG. 13.** (a) Cross-sectional view of the simulation domain for semi-annular surface wave antenna. The domain has a size of  $15 \times 7.5 \text{ cm}^2$ . (b) COMSOL free triangular generated mesh for semi-annular antenna.

$$\mu_r \left[ \frac{1}{V \cdot s \cdot \text{cm}} \right] = \frac{4.411 \cdot 10^{19}}{e^{\{0.33 \ln[1 + e^{1.5 \ln(7.721 \times 10^{-3} E_r)]\}}}, \quad (7)$$

$$T_i = T + \left( \frac{M_i + M_n}{5M_i + 3M_n} \right) \frac{M_n}{k_b} (\mu_e \cdot E) \cdot (\mu_e \cdot E). \quad (8)$$

Here,  $M_i$  is the ion mass,  $M_n$  is the mean mass of plasma,  $k_b$  is the Boltzmann constant, and  $T$  is the gas temperature. Equation (8) can be used when the reduced electric field is greater than 1000 Td, in which case it will have a different temperature value compared to the background gas temperature.

Next, laminar flow is added to the model by using computational fluid dynamic module in COMSOL. In the model, Navier-Stokes equations were used to solve single fluid flow for pressure

and velocity profiles in the chamber domain. It is assumed that the flow is laminar because Reynolds number is small for small velocities, less than  $7 \mu\text{m/s}$  and fluid is assumed to be incompressible for such small velocities as well,

$$\nabla \rho \cdot u = 0, \quad (9)$$

$$\rho \frac{\partial}{\partial t} u + \rho(u \cdot \nabla)u = \nabla \cdot [-pI + \mu(\nabla u + (\nabla u)^T)] + F. \quad (10)$$

Equations (9) and (10) are Navier-Stokes equations of continuity and momentum, respectively, where  $F$  is the volume force vector and  $\mu$  is the fluid viscosity. Mass conservation necessitates an inlet and outlet ports in the domain. The right and upper

**TABLE I.** Reaction rates of hydrogen plasma used in modeling setup and reaction rate constants are determined cross-sectional values and electron temperature.

Hydrogen reactions	Rate coefficients ( $\text{cm}^3 \text{s}^{-1}$ )	Reference
$\text{H} + \text{e} \rightarrow \text{H}^+ + 2\text{e}$ (1)	$k_1 = 6.5023 \times 10^{-9} \times T_e^{0.48931} \times e^{-12.89365/T_e}$	29
$\text{H}_2 + \text{e} \rightarrow \text{H}^+ + \text{H} + 2\text{e}$ (2)	$k_2 = 2.9962 \times 10^{-8} \times T_e^{0.44456} \times e^{-37.72836/T_e}$	30
$\text{H}_2^+ + \text{e} \rightarrow \text{H}^+ + \text{H} + \text{e}$ (3)	$k_3 = 1.0702 \times 10^{-7} \times T_e^{0.04876} \times e^{-9.69028/T_e}$	30 and 31
$\text{H}_2^+ + \text{e} \rightarrow \text{H}^+ + \text{H}^+ + 2\text{e}$ (4)	$k_4 = 2.1202 \times 10^{-9} \times T_e^{0.31394} \times e^{-23.29885/T_e}$	32 and 33
$\text{H}_2^+ + \text{H} \rightarrow \text{H}_2 + \text{H}^+$ (5)	$k_5 = 9.0 \times 10^{-10}$	32 and 33
$\text{H}_2 + \text{H}^+ \rightarrow \text{H}_2^+ + \text{H}$ (6)	$k_6 = 1.19 \times 10^{-22}$	32 and 33
$\text{H}_2 + \text{e} \rightarrow \text{H}_2^+ + 2\text{e}$ (7)	$k_7 = 3.1228 \times 10^{-8} \times T_e^{0.17156} \times e^{-20.07734/T_e}$	32 and 33
$\text{H}_3^+ + \text{e} \rightarrow \text{H}_2^+ + \text{H} + \text{e}$ (8)	$k_8 = 4.8462 \times 10^{-7} \times T_e^{-0.04975} \times e^{-19.16565/T_e}$	32 and 33
$\text{H}_2^+ + \text{e} \rightarrow \text{H}^+ + \text{H} + \text{e}$ (9)	$k_9 = 1.88 \times 10^{-13} \times T_e^{-0.39} \times e^{-28.82/T_e}$	32 and 33
$\text{H}_2 + \text{H}_2 \rightarrow \text{H}_3^+ + \text{H}$ (10)	$k_{10} = 2.6 \times 10^{-9}$	29, 34, and 35
$\text{H}_3^+ + \text{e} \rightarrow 3\text{H}$ (11)	$k_{11} = 2.19 \times 10^{-15} \times T_e^{0.8}$	30 and 29
$\text{H}_3^+ + \text{e} \rightarrow \text{H}_2 + \text{H}$ (12)	$k_{12} = 7.3 \times 10^{-16} \times T_e^{0.8}$	32, 33, and 30
$\text{H}_2 + \text{e} \rightarrow 2\text{H} + \text{e}$ (13)	$k_{13} = 1.7527 \times 10^{-7} \times T_e^{-1.23668} \times e^{-12.59243/T_e}$	32, 33, and 30

**TABLE II.** Hydrogen surface reactions considered in the simulation.

Surface reactions	Cross-sectional/rate coefficient reference
$\text{H}^+ + \text{surface} \rightarrow \text{H}$ (1)	29
$\text{H}_2^+ + \text{surface} \rightarrow \text{H}_2$ (2)	29
$\text{H}_2^+ + \text{surface} \rightarrow \text{H} + \text{H}_2$ (3)	30
$2\text{H} + \text{surface} \rightarrow \text{H}_2$ (4)	36

surfaces of the hydrogen domain, see blue area in Figs. 5 and 7, are set as inlet ports and the outlet port is the left surface of the hydrogen domain with the condition that the pressure is 1.5 Torr. Next, temperature is a factor that must be taken into account in the process of building the model and for this a heat transfer module is coupled in order to solve for the conservation of energy in all domains by utilizing conduction, convection, and radiation as the main heat transfer mechanics,

$$\rho C_p \frac{\partial}{\partial t} T + \rho C_p \mathbf{u} \cdot \nabla T + \nabla \cdot [-k \nabla T] = Q. \quad (11)$$

Equation (11), when coupled with flow velocity determines the temperature in each domain. Here,  $C_p$  is the pressure dependent heat capacity,  $k$  is the thermal conductivity,  $\rho$  is the density of a given material domain, and  $T$  is the temperature.  $Q$  is the total heat source in the model which is generated from plasma heating, electromagnetic heating, and heating from rate reactions. For the solid domains, which represent the entire system besides hydrogen domain, the second term  $\rho C_p \mathbf{u} \cdot \nabla T$  goes to zero because there is no flow. An open boundary condition is set at top and right surfaces, also those surfaces are set to be as scattering boundary conditions because the modeled domain is smaller than the entire chamber. An initial temperature is set at 293 K, and a temperature profile is generated at the end of the simulation. Also, a heat source is considered at the interface of hydrogen and solid domains where ions bombard and heat the solid surface as result of plasma-surface interactions.

The first validation test of the simulation is related to the behavior of surface wave plasma. Initially, the log of the electric field (V/m) radiates volumetrically as a conventional antenna until the critical density is achieved, and then the plasma is collapsed within the sheath behaving as evanescent EM waves. Figure 14(a)

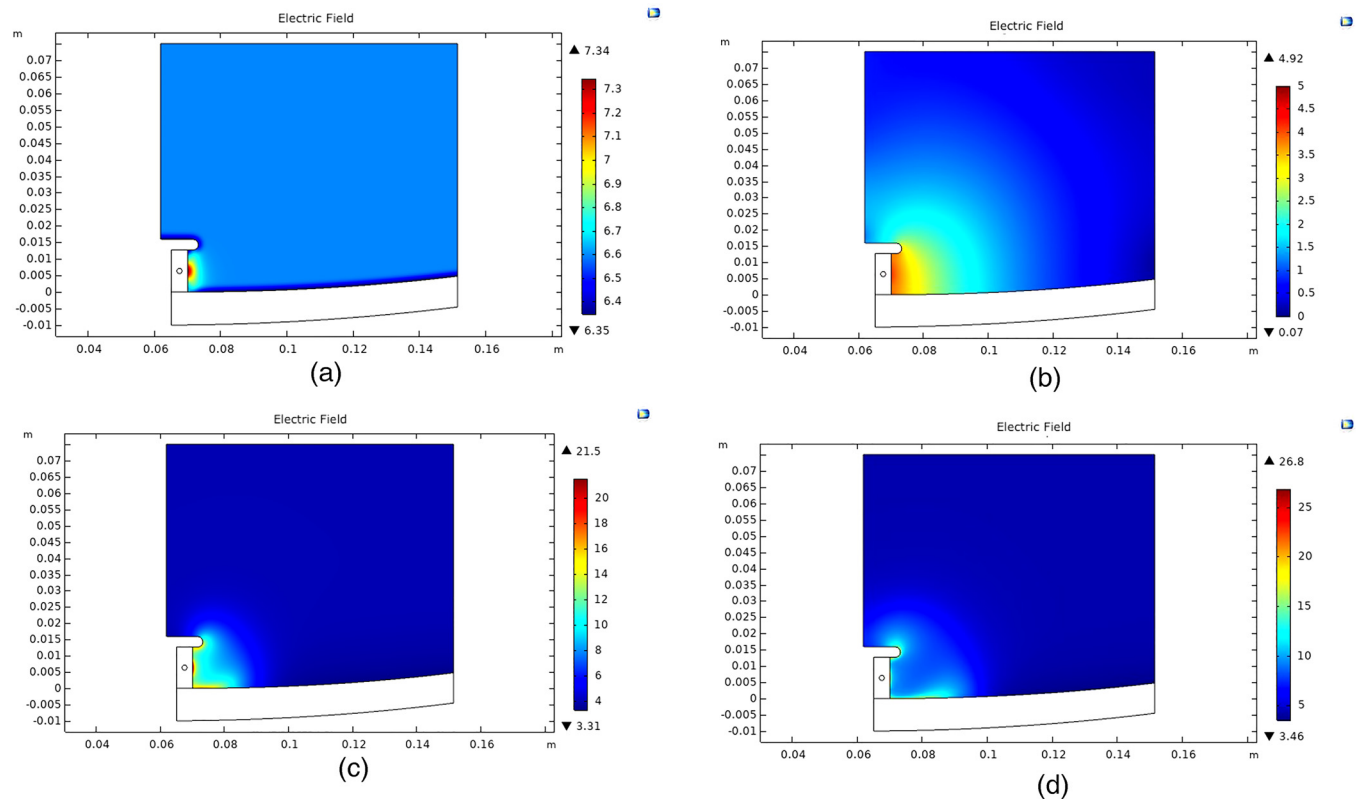


**FIG. 14.** (a) The log of the electric field (V/m) at  $t = 10^{-8}$  s. (b) The log of the electric field (V/m) at critical density at  $t = 4.7 \times 10^{-7}$  s. (c) Behavior of the log of the electric field (V/m) once it collapses to evanescent waves at  $t = 4.641 \times 10^{-7}$  s. (d) Behavior of the log of the electric field (V/m) in surface wave plasma mode simulation where the electric field is contained in the plasma sheath of the surface wave plasma at  $t = 10^{-5}$  s.



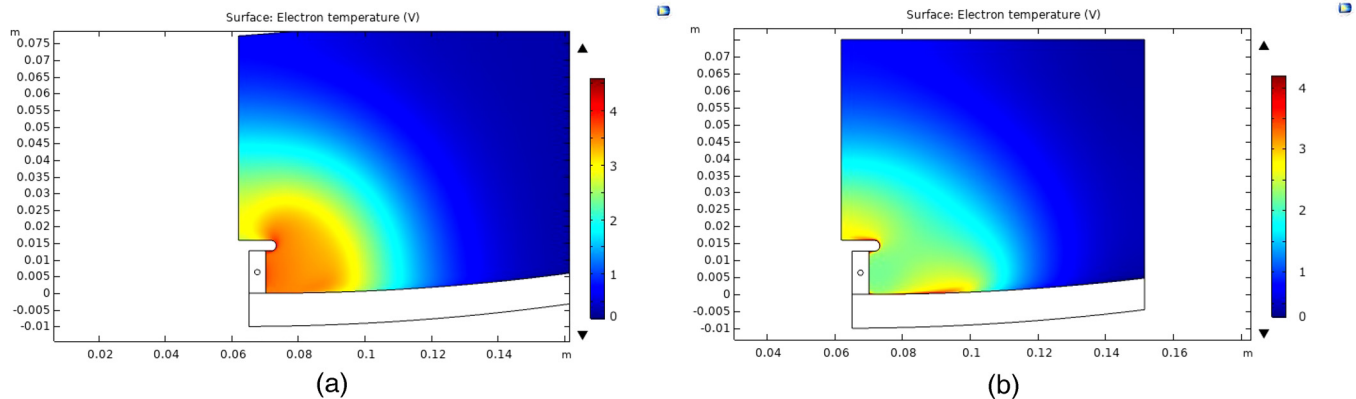


**FIG. 15.** (a) Simulation of electron temperature at the formation of critical density at  $t = 4.7 \times 10^{-7}$  s. (b) Electron temperature of the semi-annular antenna in the surface wave plasma mode with peak temperature of 6.19 eV along the surface at  $t = 10^{-5}$  s.

shows the initial formation of the electric field from the antenna, and the highest electric field radiates from the antenna at the center of the alumina ring which acts as a coaxial cable. Next, at around  $1 \mu\text{s}$ , critical density is reached at which the maximum volumetric field is achieved at the given frequency before it collapses, see Fig. 14(b). Figure 14(c) shows the behavior of the electric field in the process of collapsing in order to be confined by the plasma sheath. Finally, Fig. 14(d) shows the electric field in the surface wave plasma mode as it propagates along the surface.

The electric field simulation indicates clearly that surface wave plasma is generated in the hydrogen domain. Next, the electron temperature is shown at the moment when the critical density is reached, see Fig. 15(a). Figure 15(b) shows the behavior of the electron density during the surface wave plasma mode. Electron temperatures vary from 1 to 4 eV, with the higher values being along the surface since electron with higher energy are generated in between the critical density contour and the wall. This is also the region where the electric field is at the highest peak.

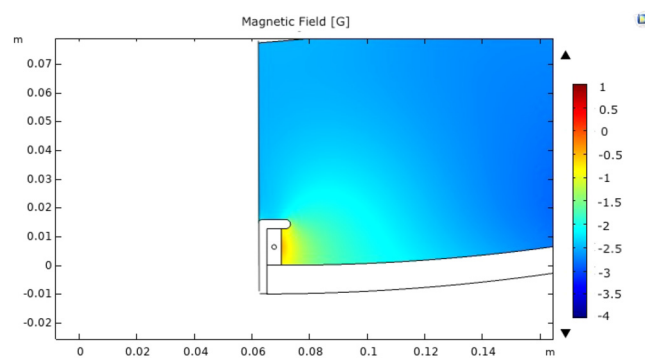


**FIG. 16.** The induced magnetic field at the end of simulation.

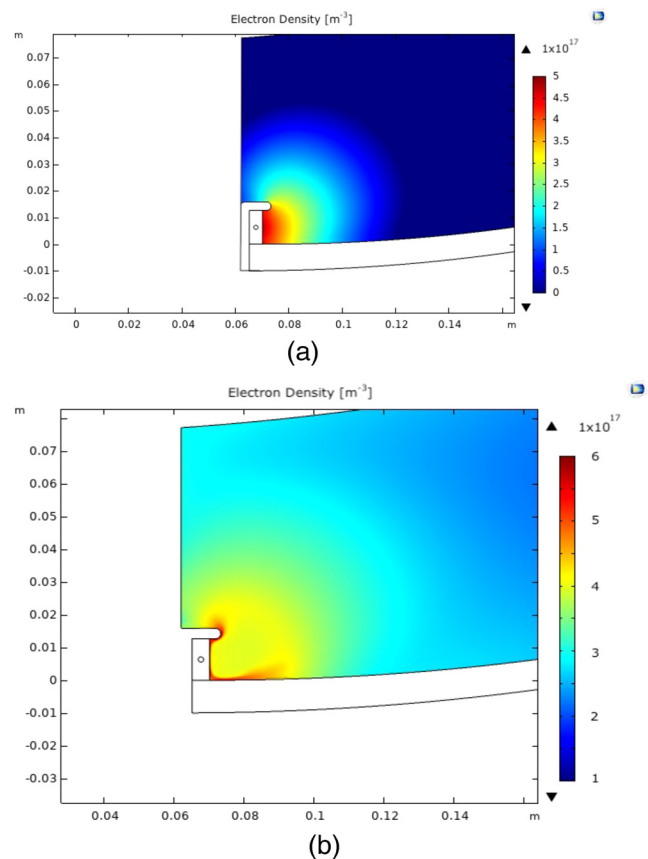


**FIG. 17.** (a) The behavior of the electron density simulation at the critical density at  $t = 4.7 \times 10^{-7}$  s. (b) The peak electron density is along the wall surfaces at the end of the simulation in the surface wave plasma mode at  $t = 10^{-5}$  s.

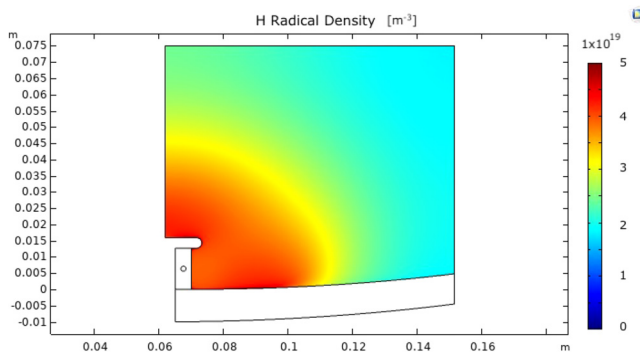


FIG. 18. Radical density distribution in the semi-circular antenna simulation.

Another important factor in the simulation process is the induced magnetic field generated by the incoming microwave. Magnetic field is indicated by Maxwell's equations, see Eqs. (2.11)–(2.14), and this induced magnetic field modifies the mobility tensor for the electrons and ions in the plasma which allows for peaks of the electron temperature.<sup>38</sup> Figure 16 shows the induced magnetic field at the end of simulation. Magnetic field is stronger closer to the antenna and since it modifies the tensor of the electron mobility, such behavior is expected.

The simulation of electron density of the surface wave plasma is shown in Fig. 17(b). The peak electron density is along the surfaces of the wall and the antenna since the density must be the highest at the skin depth of the incident wave where the power is deposited. The maximum density value is around  $6 \times 10^{17} \text{ m}^{-3}$ , which agree very well with measured density via Langmuir probe.

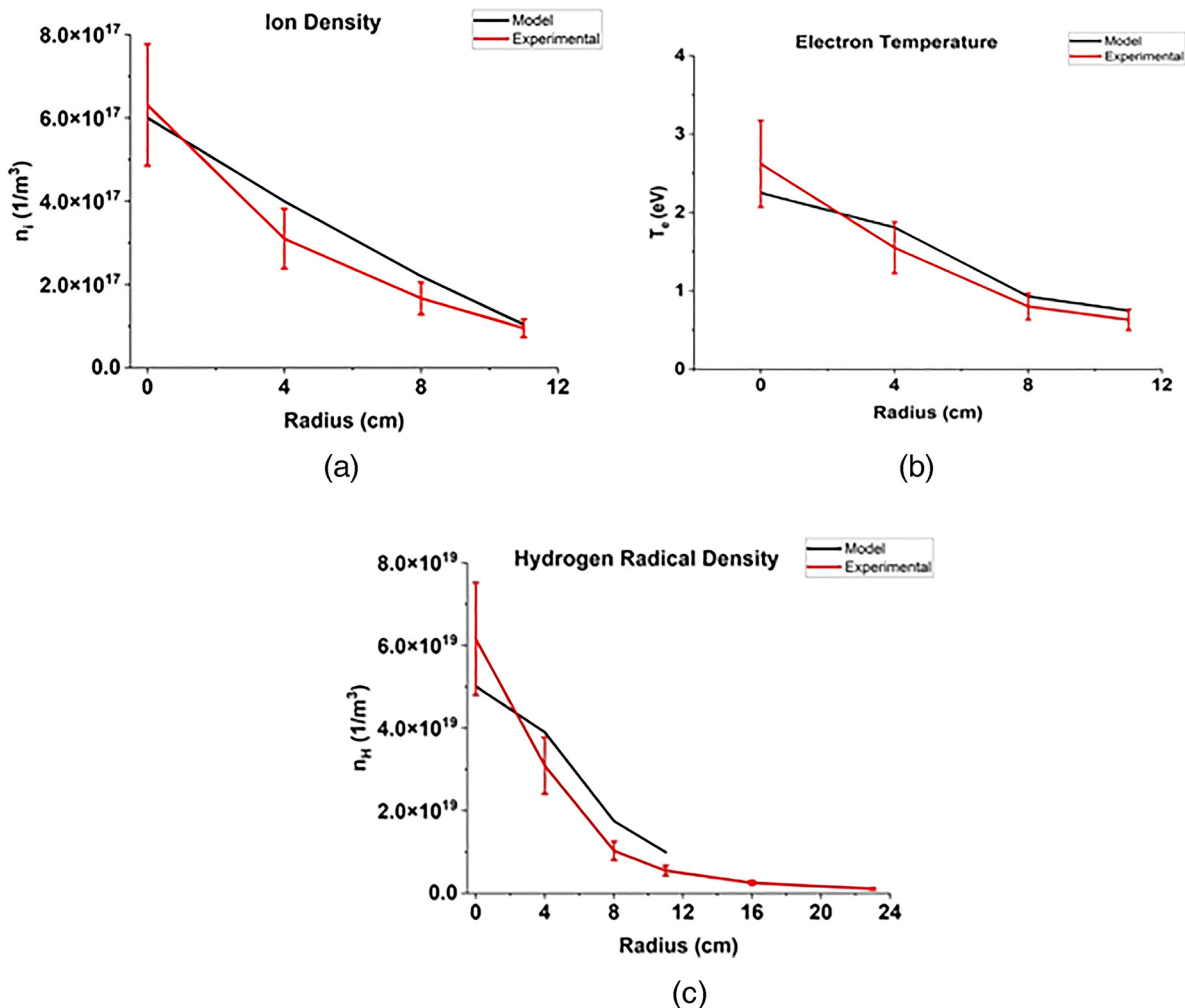


FIG. 19. COMSOL simulations and Langmuir probe measurements comparison plotted against antenna distance. (a) Electron density, (b) electron temperature, and (c) hydrogen radical density.

Figure 17(a) shows the simulation behavior at the critical density before the plasma collapses.

Finally, hydrogen radical density, see Fig. 18, is simulated which shows the peak around the area of the antenna and expanding along the surfaces. This occurs because neutral molecules are split in order to generate radicals in the bulk plasma. Radicals also stick on the wall surfaces covered with tin in order to etch the tin. The peak radical density is around  $5 \times 10^{19} \text{ m}^{-3}$  which corresponds with the measured values via radical probes. The results of COMSOL simulation seem to be in good agreement with the measured values for electron temperature and electron density. The behavior of the electric field indicates accuracy of the model since in the beginning the field has a volumetric distribution until the critical density is reached, after which the electric field collapses and it is confined in the sheath. Finally, comparison plots of electron density, electron temperature, and hydrogen radical density are shown in Fig. 19. Electron density and temperature are plotted for only first data points since the plasma model did not extend further. Model values overlay very well with experimental values, but it is worth to note that at  $r = 0 \text{ cm}$ , the model values are lower for all three graphs, however, still within the error bars. The model of the hydrogen radical density also extends for only the first four points. This comparison between measured and modeled values indicates great credibility to the COMSOL model and it can serve as an important tool for future experimental design for surface wave plasmas in order to minimize use of resources.

## V. SUMMARY AND CONCLUSIONS

EUV lithography technology is projected to take chip manufacturing below 7 nm node. One of fundamental issues of EUV lithography tools is the availability of the machine. Availability depends on a few parameters, such as mask contamination, computational lithography, resists, and collector contamination. This study focused on solving the problem of tin contamination. SWP technology is an *in situ* method in which etching occurs simultaneously while the machine is operating. The advantage of this method is the ability to generate hydrogen radicals and ions at the desired etching surface as well as high etch rates which surpass the contamination rate by a factor of 20. The objective of this study was to determine the feasibility of surface wave plasma technology in real EUV source conditions and characterize plasma parameters, such as the role the ions and radicals exhibit in the etching process.

The first experiment was to have two semi-circular antennas with two individual power feedthroughs. Each antenna is capable of running at 100 W maximum power and plasma covers the entire cone area, generating 360° of surface wave plasma. This antenna configuration underwent the most tests with varying pressure, power, flow rate, and surface temperature. Tin etch rate went from 48 nm/min at 25 W up to 270 nm/min at 100 W at the sample closest to the antenna. Again, flow rate was not a significant factor when going from 5 to 70 SLM, however, the general trend of etch rates dropping further away from the plasma is observed. In the case of varying pressure, the highest etch rate is at 0.25 Torr and the lowest at 1.5 Torr. At the lower pressure regimes, the slope of etch rate drop is smaller since there is more plasma coverage

compared to higher pressure ranges in which the plasma shrinks. In terms of surface temperature, higher etch rates are observed in lower temperatures and this behavior has been observed in linear SWP source as well. Surface temperature is not a factor in the plasma characterization in terms of ion and radical density. In the final set of tests, an additional arch antenna is installed in the outer perimeter of the collector. The goal was to create SWP in both ends of the collector and cover the entire surface between the antennas. While a bright visible plasma did not bridge between two sources due to low power input, etch rates were similar at both antennas giving a convex shape to the etching profiles. The etch rate in the middle of the collector was higher compared to the case when only cone antennas were present obtaining at least 40 nm/min at all locations. This is about 20 times greater than the expected deposition rate. If the power per source could be raised, the cleaning efficiency would be increased even further. This work shows that an EUV collector can be kept free from tin contamination by attaching a total of eight SWP sources (two to the inner cone and six to the outer perimeter). Adoption of this technique could in principle extend the collector lifetime indefinitely and, therefore, maintain high mirror reflectivity and increase EUV tool availability.

## ACKNOWLEDGMENTS

The authors are grateful for funding and support from ASML San Diego. Surface wave plasma equipment and consultations were provided by Starfire Industries. Parts of this research were carried out in the Frederick Seitz Materials Research Laboratory Central Facilities, University of Illinois, which is partially supported by the U.S. Department of Energy under Grant Nos. DE-FG02-07ER46453 and DE-FG02-07ER46471.

## AUTHOR DECLARATIONS

### Conflict of Interest

The authors have no conflicts to disclose.

### Author Contributions

**Dren Qerimi:** Data curation (equal); Formal analysis (equal); Investigation (equal); Methodology (equal); Writing – original draft (equal). **Andrew C. Herschberg:** Data curation (equal); Formal analysis (equal); Investigation (equal); Methodology (equal). **Gianluca Panici:** Data curation (equal); Formal analysis (equal); Investigation (equal); Methodology (equal); Visualization (equal). **Parker Hays:** Data curation (equal); Formal analysis (equal); Investigation (equal). **Tyler Pohlman:** Data curation (equal); Formal analysis (equal); Investigation (equal). **David N. Ruzic:** Conceptualization (equal); Data curation (equal); Formal analysis (equal); Funding acquisition (equal); Investigation (equal); Methodology (equal); Project administration (equal); Resources (equal); Supervision (equal); Validation (equal); Writing – review & editing (equal).

## DATA AVAILABILITY

The data that support the findings of this study are available within the article.

## REFERENCES

- <sup>1</sup>R. A. Burdt, Y. Tao, M. S. Tillack, S. Yuspeh, N. M. Shaikh, E. Flaxer, and F. Najmabadi, *J. Appl. Phys.* **107**, 043303 (2010).
- <sup>2</sup>J. P. Allain, M. Nieto, M. Hendricks, A. Hassanein, C. Tarrío, S. Grantham, and V. Bakshi, in *Proc. SPIE, Emerging Lithographic Technologies XI*, edited by M. J. Lercel (SPIE, San Jose, CA, 2007), p. 65171 V.
- <sup>3</sup>D. C. Brandt, I. V. Fomenkov, A. I. Ershov, W. N. Partlo, D. W. Myers, R. L. Sandstrom, N. R. Böwering, G. O. Vaschenko, O. V. Khodykin, A. N. Bykanov, S. N. Srivastava, I. Ahmad, C. Rajyaguru, D. J. Golich, S. De Dea, R. R. Hou, K. M. O'Brien, and W. J. Dunstan, in *Extreme Ultraviolet (EUV) Lithography*, edited by B. M. La Fontaine (SPIE, San Jose, CA, 2010), p. 76361I.
- <sup>4</sup>I. V. Fomenkov, A. A. Schafgans, D. C. Brandt, A. Ershov, Y. Tao, G. O. Vaschenko, and B. La Fontaine, in *EUV Lithography*, 2nd ed., edited by V. Bakshi (SPIE, Bellingham, WA, 2018), pp. 109–163.
- <sup>5</sup>H. Mizoguchi, H. Nakarai, T. Abe, K. M. Nowak, Y. Kawasuji, H. Tanaka, Y. Watanabe, T. Hori, T. Kodama, Y. Shiraishi, T. Yanagida, G. Soumagne, T. Yamada, T. Yamazaki, S. Okazaki, and T. Saitou, in *Proc. SPIE, Extreme Ultraviolet (EUV) Lithography VI*, 94220C, edited by O. R. Wood and E. M. Panning (SPIE, San Jose, CA, 2015), p. 94220C.
- <sup>6</sup>S. Yulin, N. Benoit, T. Feigl, and N. Kaiser, *Microelectron. Eng.* **83**, 692 (2006).
- <sup>7</sup>D. C. Brandt, I. V. Fomenkov, N. R. Farrar, B. La Fontaine, D. W. Myers, D. J. Brown, A. I. Ershov, N. R. Böwering, D. J. Riggs, R. J. Rafac, S. De Dea, R. Peeters, H. Meiling, N. Harned, D. Smith, A. Pirati, and R. Kazinczi, in *Proc. SPIE 9048, Extreme Ultraviolet (EUV) Lithography*, edited by O. R. Wood and E. M. Panning (SPIE, San Jose, CA, 2014), p. 90480C.
- <sup>8</sup>K. Kemp and S. Wurm, *C R Phys.* **7**, 875 (2006).
- <sup>9</sup>V. Bakshi, *EUV Lithography*, 1st ed., (SPIE, Bellingham, WA, 2008).
- <sup>10</sup>B. L. Henke, E. M. Gullikson, and J. C. Davis, *At. Data Nucl. Data Tables* **54**, 181 (1993).
- <sup>11</sup>A. A. Schafgans, D. J. Brown, I. V. Fomenkov, Y. Tao, M. Purvis, S. I. Rokitski, G. O. Vaschenko, R. J. Rafac, and D. C. Brandt, *Proc. SPIE* **10143**, 1014301 (2017).
- <sup>12</sup>R. De Bruijn, A. Bartnik, H. F. Fledderus, H. Fiedorowicz, P. Hegeman, R. C. Constantinescu, and F. Bijkerk, "Characterization of a novel double-gas-jet laser plasma EUV source," in *Proc. SPIE 3997, Emerging Lithographic Technologies IV*, (SPIE, 2000).
- <sup>13</sup>A. Takahashi, D. Nakamura, K. Tamaru, T. Akiyama, and T. Okada, *Appl. Phys. B* **92**, 73 (2008).
- <sup>14</sup>M. M. J. W. van Herpen, D. J. W. Klunder, W. A. Soer, R. Moors, and V. Banine, *Chem. Phys. Lett.* **484**, 197 (2010).
- <sup>15</sup>D. T. Elg, J. R. Sporre, G. A. Panici, S. N. Srivastava, and D. N. Ruzic, *J. Vac. Sci. Technol. A* **34**, 021305 (2016).
- <sup>16</sup>T. Yanagida, H. Nagano, Y. Wada, T. Yabu, S. Nagai, G. Soumagne, T. Hori, K. Kakizaki, A. Sumitani, J. Fujimoto, H. Mizoguchi, and A. Endo, in *Proc. SPIE, Extreme Ultraviolet (EUV) Lithography II*, edited by B. M. La Fontaine and P. P. Naulleau (SPIE, San Jose, CA, 2011), p. 79692 T.
- <sup>17</sup>D. N. Ruzic, *Electric Probes for Low Temperature Plasmas* (American Vacuum Society, New York, 1994).
- <sup>18</sup>D. Qerimi, G. A. Panici, A. Jain, D. Jaconson, and D. N. Ruzic, *J. Vac. Sci. Technol. A* **39**, 023004 (2021).
- <sup>19</sup>D. Qerimi, I. Shchelkanov, G. A. Panici, A. Jain, J. Wagner, and D. N. Ruzic, *J. Vac. Sci. Technol. A* **39**, 023003 (2021).
- <sup>20</sup>D. T. Elg, G. A. Panici, S. Liu, G. Girolami, S. N. Srivastava, and D. N. Ruzic, *Plasma Chem. Plasma Process.* **38**, 223 (2018).
- <sup>21</sup>D. Qerimi, G. Panici, A. Jain, D. Jacobson, and D. N. Ruzic, *J. Vac. Sci. Technol. B* **38**, 052601 (2020).
- <sup>22</sup>G. Panici, *Hydrogen Surface Wave Plasma Cleaning of the EUV Collector* (University of Illinois at Urbana-Champaign, 2021).
- <sup>23</sup>R. F. Pfaff, *The FAST Mission* (Springer Netherlands, Dordrecht, 2001).
- <sup>24</sup>B. Li, H. Li, H. Wang, J. Xie, and W. Liu, *J. Appl. Phys.* **110**, 073308 (2011).
- <sup>25</sup>S. V. Bulanov, T. Zh. Esirkepov, M. Kando, J. K. Koga, T. Hosokai, A. G. Zhidkov, and R. Kodama, *Phys. Plasmas* **20**, 083113 (2013).
- <sup>26</sup>H.-M. Yin, *SIAM J. Math. Anal.* **29**, 637 (1998).
- <sup>27</sup>H.-M. Yin, *Eur. J. Appl. Math.* **5**, 57 (1994).
- <sup>28</sup>J. Rautio, *IEEE Spectrum* **51**, 36 (2014).
- <sup>29</sup>R. Janev, R. Detlev, and S. Ulrich, *Collision Processes in Low-Temperature Hydrogen Plasmas* (Germany, 2003).
- <sup>30</sup>I. Méndez, F. J. Gordillo-Vázquez, V. J. Herrero, and I. Tanarro, *J. Phys. Chem. A* **110**, 6060 (2006).
- <sup>31</sup>T. Body, S. Cousens, J. Kirby, and C. Corr, *Plasma Phys. Control. Fusion* **60**, 075011 (2018).
- <sup>32</sup>N. Fu, Y. Liu, X. Ma, and Z. Chen, *J. Microelectron. Manuf.* **2**, 1 (2019).
- <sup>33</sup>E. Bloyet, P. Leprince, and M. L. Blasco, *Phys. Lett. A* **83**, 391 (1981).
- <sup>34</sup>S. Kim, M. A. Lieberman, A. J. Lichtenberg, and J. T. Gudmundsson, *J. Vac. Sci. Technol. A* **24**, 2025 (2006).
- <sup>35</sup>A. T. Hjartarson, E. G. Thorsteinsson, and J. T. Gudmundsson, *Plasma Sources Sci. Technol.* **19**, 065008 (2010).
- <sup>36</sup>D. Qerimi, *Radical Probe System for In-Situ Measurements of Radical Densities of Hydrogen, Oxygen and Nitrogen* (University of Illinois at Urbana-Champaign, 2019).
- <sup>37</sup>T. Piskin, S. O. Macheret, and J. Poggie, *AIAA Aviation 2019 Forum* (American Institute of Aeronautics and Astronautics, Dallas, TX, 2019).
- <sup>38</sup>M. A. Lieberman and A. J. Lichtenberg, *Principles of Plasma Discharges and Materials Processing: Lieberman/Plasma 2e* (John Wiley & Sons, Inc., Hoboken, NJ, 2005).